The Structure of the Martian Quasi-perpendicular Supercritical Shock as seen by MAVEN

Sofía Burne[1], Cesar Bertucci[1], Christian Xavier Mazelle[2], Laura Fernanda Morales[3], Karim Meziane[4], Jared Randolph Espley[5], Jasper S. Halekas[6], David L. Mitchell[7], and Emmanuel Penou[8]

[1]Institute for Astronomy and Space Physics - IAFE
[2]IRAP; Université de Toulouse; CNRS; CNES; UPS-OMP; Toulouse, France
[3]Instituto de Física del Plasma
[4]University of New Brunswick
[5]NASA Goddard
[6]University of Iowa
[7]University of California, Berkeley
[8]IRAP

November 24, 2022

Abstract

The Martian bow shock is a rich example of a supercritical, mass-loaded collisionless shock that coexists with ultra-low frequency upstream waves that are generated by the pick-up of exospheric ions. Its small size (comparable with the solar wind ion gyroradius) raises questions related to which particle acceleration and energy dissipation mechanism can take place. The study of the Martian shock structure is crucial to comprehend its microphysics and is of special interest to understand the solar wind - planet interaction with a virtually unmagnetized body. We report on a complete identification and first characterization of the supercritical substructures of the Martian quasi-perpendicular shock, under the assumption of a moving shock layer, using MAVEN magnetic field and solar wind plasma observations for two examples of shock crossings. We obtained substructures length-scales comparable from those of the Terrestrial shock, with a narrow shock ramp of the order of a few electron inertial lengths. We also observed a well defined foot (smaller than the proton convected gyroradius) and overshoot that confirm the importance of ion dynamics for dissipative effects.

The Structure of the Martian Quasi-perpendicular Supercritical Shock as seen by MAVEN

S. Burne[1], C. Bertucci[1], C. Mazelle[2], L. F. Morales[3], K. Meziane[4], J. Espley[5], J. Halekas[6], D. Mitchell[7], E. Penou[2]

[1]IAFE, UBA CONICET, Buenos Aires, Argentina
[2]IRAP, UPS CNRS CNES, Toulouse, France
[3]INFIP, UBA CONICET, Buenos Aires, Argentina
[4]University of New Brunswick, Fredericton, New Brunswick, Canada
[5]NASA Goddard Space Center, Greenbelt, MD, USA
[6]University of Iowa, Iowa City, USA
[7]SSL, UC Berkeley, Berkeley CA, USA

Key Points:

- A new methodology to identify the supercritical quasi-perpendicular shock substructures is applied to Martian bow shock
- All three supercritical substructures are identified and their thickness is derived for the first time using an estimated shock speed
- The reported ramp width is comparable with the electron inertial length which is compatible with Earth observations

Corresponding author: Sofía Burne, `sburne@iafe.uba.ar`

Abstract

The Martian bow shock is a rich example of a supercritical, mass-loaded collisionless shock that coexists with ultra-low frequency upstream waves that are generated by the pick-up of exospheric ions. Its small size (comparable with the solar wind ion gyroradius) raises questions related to which particle acceleration and energy dissipation mechanism can take place. The study of the Martian shock structure is crucial to comprehend its microphysics and is of special interest to understand the solar wind - planet interaction with a virtually unmagnetized body. We report on a complete identification and first characterization of the supercritical substructures of the Martian quasi-perpendicular shock, under the assumption of a moving shock layer, using MAVEN magnetic field and solar wind plasma observations for two examples of shock crossings. We obtained substructures length-scales comparable from those of the Terrestrial shock, with a narrow shock ramp of the order of a few electron inertial lengths. We also observed a well defined foot (smaller than the proton convected gyroradius) and overshoot that confirm the importance of ion dynamics for dissipative effects.

Plain Language Summary

The supermagnetosonic solar wind interacts with the Martian plasma environment and forms a shock wave so it can decelerate and divert the planetary obstacle. Depending on the orientation of the interplanetary magnetic field and the strength of the incident solar wind flow, there are different mechanisms responsible for the dissipation that transforms the solar wind kinetic energy into heat. To understand these mechanisms, it is crucial to study the shock structure. In this paper we analyze the structure of the Martian supercritical quasi-perpendicular shock using MAVEN measurements, and find consistent results with the Terrestrial bow shock, despite the differences with the Martian - solar wind interaction.

1 Introduction

The presence of collisionless bow shocks around the solar system (e.g., Russell et al., 1985, and references therein) is one of the clearest manifestations of the supermagnetosonic nature of the solar wind (SW) plasma. The function of planetary shocks is to decelerate the upstream plasma flow down to local submagnetosonic speeds. This is achieved through complex, nonlinear processes where the upstream flow kinetic energy is lost to dissipation and dispersion (Treumann, 2009).

Most solar system shocks are supercritical (e.g., Sulaiman et al., 2015; Bertucci et al., 2015). This means that above a critical shock strength of typically $M_A \sim 3$ (Edmiston & Kennel, 1984), resistivity alone cannot provide the necessary steepening to satisfy the Rankine-Hugoniot jump conditions because dissipation timescales are too long for a stationary shock to convert the excess kinetic energy into heat (Marshall, 1955; Kantrowitz et al., 1966). As additional mechanisms are necessary to slow down the flow, a fraction of the incoming plasma is reflected upstream. The reflected ions gyrate about the magnetic field lines in the plasma rest frame (Leroy et al., 1981; Paschmann et al., 1982; Sckopke et al., 1983), which means in perpendicular or quasi-perpendicular (Q$\perp$) crossings (with shock normal angles θ_{Bn} over 45°) they mostly return to the shock front after a partial gyration in the upstream region. As they make their way back, they accelerate and generate currents that modify the magnetic field profile, forming the characteristic foot, ramp, and overshoot to ensure energy dissipation.

Woods (1969, 1971) first described the foot formation by the specular reflection of the SW ions and estimated its width at $\sim$ 0.7 upstream convected proton gyroradius ($r_{ci} = V_u/\omega_{ci}$) for the strictly perpendicular crossing. Livesey et al. (1984) and Gosling and Thomsen (1985) later generalized this initial study to arbitrary shock geometries.

Hybrid simulations (Leroy et al., 1982) and Earth studies (Livesey et al., 1982; Scudder et al., 1986; Mellott & Livesey, 1987) showed the overshoot amplitude increases with the strength of the shock (M_A) and has a typical thickness of about 4 - 7 upstream ion inertial lengths (c/ω_{pi}) or 1 - 3 r_{ci}. Moreover, Scudder et al. (1986) and Newbury and Russell (1996) reported a magnetic ramp of a fraction of c/ω_{pi}, which questioned the set idea that the typical shock ramp scaled with the ion skin depth (e.g., Russell & Greenstadt, 1979). More recent studies, however, found the ramp can be as small as a few electron inertial lengths (c/ω_{pe}) (Mazelle et al., 2010; Yang et al., 2013). Finally, hybrid and PIC simulations (Leroy et al., 1982; Leroy, 1983; Hada et al., 2003; Lembège et al., 2009; Yang et al., 2009) and a few observational studies at Earth (e.g., Mazelle et al., 2010; Dimmock et al., 2019; Mazelle & Lembège, 2020) showed that for relatively low upstream ion beta the foot, ramp and overshoot are non-stationary features and lead to a continuous self-reformation of the shock structure on gyro-scales of the incoming ions.

The study of the shock substructures is fundamental to understand the local particle acceleration and energy dissipation mechanism that arise at the shock front of a supercritical transition, as their characteristic scales are intimately connected to particle dynamics. However, few studies of extraterrestrial planetary bow shocks can be found in the literature. Achilleos et al. (2006) reported ramp widths between $0.1{-}1$ c/ω_{pi} that suggested the dominance of ion kinetics in energy dissipation processes in the highly supercritical Kronian bow shock. Other works include Giagkiozis et al. (2017) measurement of ramp widths of ~ 3 c/ω_{pe} for the Venusian shock, or Moses et al. (1985) analysis of electron heating generated by ion reflection at the foot of the Jovian shock.

As anticipated by Moses et al. (1988), the Martian bow shock is a particularly interesting study case. Mars lack of an intrinsic magnetic field means its interaction with the SW plasma is more Venus or comet-like than Earth-like. The primary obstacle to the supermagnetosonic flow is formed by mass loading and induction at the magnetosphere, with small contributions of crustal magnetic fields (Gruesbeck et al., 2018). In addition, Mars small size coupled with the low interplanetary magnetic field (IMF) strength at its heliocentric distance results in a shock and magnetosheath thickness comparable with SW ion scale-lengths. This translates into insufficient space for complete thermalization of the SW before encountering the obstacle, and kinetic effects are potentially more relevant (Moses et al., 1988). Finally, the planet's weak gravitational field results in a widely extended exosphere, which means heavy ions and protons of exospheric origin are encountered far beyond the shock boundary. This makes for a very distinct upstream environment as the pick-up of newborn planetary ions results in high amplitude ultra-low frequency (ULF) waves that could "anticipate" the SW of the presence of the planetary obstacle and slow it down sooner (as was long thought for the SW-asteroid interaction). These waves have an even spatial distribution (Mazelle et al., 2004) and peak-to-peak magnetic amplitudes comparable with the background magnetic field, which usually interfere with the supercritical Q$\perp$ shock structure and could potentially modify it.

The first observations of the Martian bow shock were obtained with Mariner 4 (Smith et al., 1965) and early Soviet missions (Zakharov, 1992, and references therein), which provided basic parameters of the boundary. Phobos 2 revealed a high-level upstream wave activity (Russell et al., 1990; Sagdeev et al., 1990; Delva & Dubinin, 1998), and allowed for the first studies of the supercritical Q$\perp$ substructures. Schwingenschuh et al. (1990) provided a first view of the magnetic morphology of the shock, finding a minimum foot size of 1350 km; and Sagdeev et al. (1990) estimated a foot width of ~ 1.3 r_{ci}. Tatrallyay et al. (1997) investigated the overshoot under the assumption of a stationary shock, reporting a dependence of its amplitude with the magnetosonic Mach number and a typical width of $0.5 - 2.5$ r_{ci} or $2 - 8$ c/ω_{pi}. MGS and MEX filled in more details to the Martian shock study, with close-in magnetic field data (Acuña et al., 1998) and plasma measurements around the planet (Fränz et al., 2007).

Since 2014, the Mars Volatile EvolutioN (MAVEN) mission (Jakosky et al., 2015) is providing simultaneous high-time resolution magnetic field and plasma measurements with an unprecedented coverage of the Martian space environment. Several works have already made use of MAVEN's capabilities to enrich our understanding of the Martian shock and its upstream phenomena (e.g., Meziane et al., 2017, 2019; Mazelle et al., 2018). In particular, Madanian et al. (2020) study of the shock's non-stationarity refers to the Martian substructures, though without any specifics about the identification criteria or their characterization. Therefore, a complete characterization of the Q$\perp$ supercritical shock structure remains. The aim of this study is to provide an in-depth analysis of the Martian Q$\perp$ shock structure using MAVEN dataset to optimize its characterization in spite of the limitations imposed by single-spacecraft observations, the shock's non-stationarity and the colocation of ULF waves. This is the first time all three supercritical substructures are characterized for the Martian shock, especially assuming a moving shock front. Moreover, we applied a detailed methodology for data processing and set clear criteria for the substructures identification, something that can be unclear in some previous works (Mazelle et al., 2010).

The paper is structured as follows. MAVEN on-board instruments are described in section 2, and the methodology is introduced in section 3. We follow with the observations and results in section 4, and in section 5 we present the final remarks and conclusions.

2 MAVEN On-board Instruments

Our study of the Martian shock Q$\perp$ structure is based on magnetic field and plasma data from MAVEN fluxgate magnetometer (MAG) (Connerney et al., 2015a, 2015b), the Solar Wind Ion Analyzer (SWIA) (Halekas et al., 2015, 2017) and the Solar Wind Electron Analyzer (SWEA) (Mitchell et al., 2016).

MAG is a dual fluxgate magnetometer that samples the ambient magnetic field vector with a time resolutions of up to 32 Hz, a 0.008 nT resolution and an minimum accuracy of 0.05%. We used the Mars Solar Orbital (MSO) system of coordinates, where the X-axis points sunward, the Y-axis is anti-parallel to the planet's orbital motion, and the Z-axis completes the right-hand triad.

SWEA is a hemispheric electrostatic analyzer designed to measure the energy and angular distribution of electrons in the 3-4600 eV energy range, with a resolution of 17% ($\Delta E/E$) and a maximum cadence of 2 s. It swipes almost all 4π of solid angle with a 22.5° angular resolution in the azimuth direction and 20° along the direction of the elevation angle. As MAVEN is a 3-axis stabilized spacecraft, the $360° \times 7°$ field of view is broaden up to $360° \times 120°$ by the use of electrostatic deflectors, covering 87% of the sky.

SWIA is a hemispheric electrostatic analyzer with cylindrical symmetry that provides high cadence measurements of solar wind ion velocity distributions between 5-25000 eV, with energy resolution of 14.5%. It has an active angular field of $360° \times 90°$ with a resolution of $3.75° \times 4.5°$ sun-ward and $22.5° \times 22.5°$ in all other directions, and allows a $\pm 45°$ aperture along the elevation angle by the use of electrostatic deflectors. SWIA returns fine (SWIFA) and coarse (SWICA) 3-D velocity distribution function moments and spectra, as well as on-board computed measurements.

The fine and coarse data products cannot be used indistinctly and must be carefully considered depending on the plasma region being studied to avoid inaccurate measurements (Halekas et al., 2017). SWIFA has a narrow field of view (FOV) that covers a limited angular range around the peak of the ion distribution and allows to properly resolve the collimated SW beam before the shock. SWICA has a wide FOV better suited to measure the shocked plasma in the magnetosheath, which has a wider phase distribution. Also, on-board computed quantities are not always reliable. Their computation depends on the automated telemetry mode selection that determines which data products are combined. The on-board data near telemetry switches (that are common near the shock transition) must be considered with caution as they can introduce non-physical discontinuities.

In the SW and magetosheath regions, protons constitute a 90% of the ion population. The rest corresponds to heavier ions, of which alpha particles provide the most significant contribution. The trace presence of alpha particles barely affects the calculation of the density and velocity moments, but they do artificially increase the temperature moment (Halekas et al., 2017). To obtain a correct proton temperature, the alpha particles are removed from the ion distribution by introducing an upper energy bound separating the protons from alpha particles. This threshold energy is identified upstream with fine measurements. Downstream from the shock, the different ions contributions mix up and an upper limit of the total ion temperature can be estimated from the coarse data.

3 Methodology

The identification of the shock foot, ramp and overshoot in the time series is based on the multi-spacecraft analysis by Mazelle et al. (2010) and Mazelle and Lembège (2020). Following this work, we determine a temporal error bar (defined by an outer and inner edge) to mark the beginning of a substructure, and another temporal error bar to mark its end. In particular, the end of the foot matches the start of the ramp, and the end of the ramp matches the start of the overshoot. This delimitation is first done by visual inspection and later refined by an automated algorithm. The methodology is also similar to that used in Achilleos et al. (2006).

For the foot start, high and lower resolution magnetic field data are used to isolate the foot signature from the quasi-monochromatic upstream wave field. In the observational analysis, this was done by identifying two features: (1) an unambiguous increase in the upstream background field strength (indicative of the plasma compression at the shock), and (2) the loss of coherence of the upstream waves (as they colocate with the shock structure and shock derived instabilities). The automated algorithm accounts for these traces by identifying the times when the magnetic field magnitude and components surpass the upstream asymptotic values B_u and $B_{x_i u}$, respectively, in a 4σ level. The earliest time defines the outer edge of the error bar and the latest, the inner edge. The 4σ level reference is considered representative of the field variation due to the shock's compression. This modification from the 3σ level proposed by Mazelle et al. (2010), accounts for a higher variability upstream of the shock, given the presence of high amplitude waves.

For the overshoot end, the observational references to mark the outer and inner edges are: (1) the end of the highest amplitude perturbations that constitute the first and main overshoot, and (2) the inflection point towards the first undershoot. Working with different time resolution data is useful to filter the upstream waves that go through the shock and mix with the lower-resolution overshoot structure. The refining algorithm searches for the times when the magnetic field magnitude falls below the $\pm5\%$ level from the nominal downstream value B_d. As the downstream region is more variable, a 5% variation is considered enough to account for the deviation from the asymptotic field representative of the overshoot boost. This criterion, similar to that used at Earth, is thought equally useful for the Martian shock as long as the overlapping of high-amplitude upstream waves does not interfere with the search condition (i.e. if the algorithm works on filtered or averaged data).

For the ramp, the initial delimitation considers a time interval that contains the transition from foot to overshoot through a (in-average) monotonic ascending curve of the background magnetic field magnitude. To properly resolve the ramp, it is crucial to work with the highest resolution data available, as the sudden shock jump means a lower density of data points. To refine the end error bar, an algorithm searches for the times when the magnetic field magnitude surpasses the downstream asymptotic value B_d in $\pm 5\%$. As this also delimits the start of the overshoot, it is meant to be consistent with the reference that was set to mark the overshoot end. A second algorithm finds the best linear regression of the data points contained within the initial start error bar and the already-refined end error bar, allowing for a variation of the fitting interval within these limits. The time interval associated with the linear fit with the highest adjusted r-square (and fitting at least 4 data points) is used to refine either the outer or the inner edge of the start error bar, as well as the outer or inner edge of the end error bar.

Once the temporal widths of the substructures are determined in the MAVEN time series, their 'real' thicknesses can be obtained by estimating the shock speed relative to the spacecraft. Within the limitations of a single-spacecraft mission, the shock speed is assumed to be constant as a step further from the static bow shock boundary assumption (e.g., Tatrallyay et al., 1997). We followed Gosling and Thomsen (1985) to estimate the speed of the shock by combining the observations of the foot's traversal time and an analytical expression for its thickness. This analytical expression is based on the calculation of the full particle trajectory, and associates the foot width to the distanced covered in the turnaround time. The method assumes that the same speed applies to the whole shock structure, thus providing the shock speed along its normal.

4 Observations and Results

4.1 Dec 25, 2014 event

We analyzed the structure of the Martian shock as seen by the MAVEN spacecraft on December 25, 2014, arround the shock crossing at 9:49:10 UTC and a solar zenith angle $SZA = 85°$. Figure 1 shows time series of MAVEN MAG, SWIA and SWEA data around the shock crossing as the spacecraft dives into the Martian magnetosphere. All vector magnitudes are represented in MSO coordinates.

We used fully-calibrated, Level 2 SWIFA and SWICA ion moments to compute upstream and downstream parameters, respectively, and plotted both SWIFA and SWICA moments upstream from the shock for comparison. The upstream ion temperatures are computed from the core proton distributions, avoiding the effect due to the presence of alpha particles. To isolate the core proton population, we only considered the ion distribution in the 300 - 1000 eV energy range. Dowsntream, the temperatures are calculated from the full ion distributions using SWICA measurements. The ion densities and velocities also correspond to the full ion distribution (from SWIFA upstream and SWICA downstream). Here, alpha particle contribution is negligible, therefore the core proton distribution is representative of the total ion population.

Electron moments need also to be processed carefully. In particular, they need to be corrected for the spacecraft potential (Mitchell et al., 2016). For this event, the spacecraft potential was not specified in the MAVEN data repository. Therefore, we set an upstream potential value of 1 eV and downstream value of 5 eV, so as to satisfy quasi-neutrality of the plasma. The resulting electron temperature is shown on Figure 1.

In the figure, we see the shock transition is characterized by an increase of the ion and electron densities resulted from the plasma compression. There is also an increase in the plasma temperature and in the flux of suprathermal electrons, as the particles heat up converting their kinetic energy into heat and decreasing the mean plasma speed. The latter is evident in the deceleration of the SW ions, that indicates the plasma transition into a sub-magnetosonic regime to allow the flow to change its direction and divert around the planet (as seen in the change in SW ion velocity components). In the bottom panels (that show MAG data at 32 Hz and 1 Hz resolution, and averaged every ~ 30 s with moving averages) two shock features appear distinctively. First, the sudden increase of the IMF strength typical of fast magnetosonic shocks (e.g., Burgess, 1995), where low magnetic diffusion (or high conductivity) means the SW flow carries the magnetic field lines with it. Second, the presence of primary and secondary overshoots underneath the wave field that evidence the presence of kinetic mechanisms of energy dissipation that attempt to (partially) thermalize the plasma downstream. These substructures, in addition to the ramp and the foot (more visible in higher resolution data) are characteristic attributes of supercritical Q$\perp$ shocks.

4.1.1 Plasma and Field Parameters

In order to characterize the shock's initial and final plasma states, we selected upstream and downstream time intervals by visual inspection with the following criteria: (1) the intervals should be as temporally close as possible to the shock transition (to select asymptotic regions of the same shock layer and avoid effects due to the significant curvature of the Martian shock and inhomogeneities of the plasma and field environment); (2) they should show a relatively small variability on the macroscopic plasma parameters; (3) they should exclude the shock and its substructures; and (4) they should be wide enough to provide representative average parameters (e.g., to make the ULF upstream wavefields cancel out), without extending too far from the shock. Our methodology aligns with the criteria of Horbury et al. (2002).

The selected upstream and downstream intervals for this shock crossing are 9:45:07-9:48:41 and 9:56:31-10:01:42 UTC respectively (shaded areas in Figure 1). The corresponding average plasma and field parameters are summarized in Table 1 and are comparable with the ones reported by Gruesbeck et al. (2018) for this same shock crossing. The average ion velocities shown on the table and used in the remaining of this work were calculated from the Level 2 on-board SWIA velocity moment, which reported good quality-flags in the selected intervals (Halekas et al., 2017) and showed no significant differences with the corresponding mean values calculated from the fine and coarse products in the upstream and downstream intervals, respectively. The rest of the ion and electron average moments were derived from the corresponding time series illustrated in Figure 1 for the selected intervals.

Based on these results, we characterized the incoming SW by calculating additional fundamental parameters. We obtained a cone angle between the upstream magnetic field and ion velocity $\alpha_{cone} = 56°$. For the upstream Alfvén speed we used the expression $V_A = B_u/\sqrt{\mu_0 \rho_u}$, with $\rho_u = m_p n_{pu} + 4 m_p n_{\alpha u}$ the ion upstream mass-density, and obtained $V_A = 37.8$ km/s. Though the density of alpha particles is generally low, it can be significant when computing quantities that depend on the total ion mass density. However, for this particular event the density of H_e^{++} was lower than 0.05% and made no significant contribution to V_A. The upstream sound speed, estimated as $\sqrt{(T_e + 2T_i)/m_p}$, yields $V_{cs} = 39.2$ km/s. The upstream fast magnetosonic speed $\sqrt{V_A^2 + V_{cs}^2}$, is $V_f = 54.5$ km/s.

The normal vector to the shock crossing $\hat{N} = (0.71, 0.36, -0.60)$ was estimated as an average of the vectors derived from the coplanarity mixed-modes (Schwartz, 1998) and the re-adjusted geometric bow shock model (Vignes et al., 2000), which we found to be the best normal vector estimations in comparison with the Magnetic Coplanarity Normal (Schwartz, 1998) and the Minimum Variance Analysis (Sonnerup & Scheible, 1998). This shock normal has an angular uncertainty of 8° and forms a shock normal angle $\theta_{B_u N} = (78 \pm 3)°$. We used this vector to obtain the shock Mach numbers $M_{cs} = 6.0$, $M_A = 6.2$ and $M_f = 4.3$, which clearly indicate the shock is in a supercritical regime.

4.1.2 Identification of the Foot, Ramp and Overshoot

Figure 2 (a) shows magnetic field data around the outer edge of the shock and at the foot. The four bottom panels show MAG high time resolution data, where it is hard to identify the start of the foot signature because of the presence of upstream waves at the local proton cyclotron frequency. The following upper panel shows the magnetic field residuals δB (of 1 s resolution) after subtracting the moving average magnetic field strength B, with time windows of 20, 30 and 40 s (that is, multiples of the upstream proton cyclotron period). At the top panel we show the spectogram of the B_z component superimposed with the instantaneous proton cyclotron frequency.

The initial (visual) delimitation of the foot start error bar is given by its outer and inner limits (FS1e and FS2e) which follow the methodology in section 3. The signature shock compression of the IMF is observed as an increase in the magnetic field strength and as a baseline shift on the residual curves of B for the different averaging time windows. On the other hand, the disruption of the quasi-monochromatic behavior of the upstream waves can be seen on the broadening of the frequency spectrum (overlooking the poorer time resolution). Upstream from the shock, the strongest spectral densities mainly concentrate around the $\sim$ 0.1 Hz of the upstream proton cyclotron frequency. But as the foot edge is approached, we see not only contributions from the $\sim$ 2 Hz wave packets (possibly resulted from a dispersion at the steepened fronts of the upstream waves), but also from other frequencies. The broadening of the spectrum becomes more evident around the inner edge. There is also an increase in the electron density, that becomes more evident as MAVEN moves deeper into the foot structure. For the automated delimitation, the algorithm worked on the high-resolution magnetic field data, allowing for a 2 s margin outside the initial error bar. The x_{MSO} field component did not contribute to the refinement of the time limits, as it did not satisfy the search condition. The final foot start error bar is delimited by solid lines on Figure 2 (a), with FS1a the final outer edge and FS2a the final inner edge.

Figure 2 (b) shows the delimitation of the overshoot end on magnetic field strength at 32 Hz resolution, 1 Hz resolution, and averaged every 20 and 40 s, magnetic field components at 1 Hz resolution, and electron fluxes. The initial outer and inner limits are noted OE1e and OE2e, respectively. As the overshoots have longer apparent timescales than the upstream waves period in the spacecraft frame, they are more identifiable in lower time resolution data. For this reason (and as explained in section 3), the automated algorithm was set to work on the magnetic field magnitude averaged every 2 cyclotron periods (20 s for this crossing) so as to avoid the effect of the upstream waves that go through the shock while still not over-softening the profile. A 10 s margin outside the initial error bar was allowed. If we had worked with the highest resolution data instead, the higher frequency oscillations would have dominated and rapidly saturated the search. The final error bar is marked with solid lines on Figure 2 (b), with OE1a the final outer edge and OE2a the final inner edge.

The ramp delimitation is shown in Figure 2 (c). The initial error bars is given by the first pair of dashed lines, with RS1e the outer edge and RS2e the inner edge; and the initial ramp end is given by the second pair of dashed lines, with RE1e the outer edge and RE2e the inner edge. The final start error bar is delimited by the first pair of solid lines, with RS1a the outer edge and RS2a the inner edge. RS1a was obtained by finding the measured data point closest to RS1e, and RS2a is given by the beginning of the interval that allows for the best linear fit of the data points. The final end error bar is marked by the second pair of solid lines, with RE1a the outer edge and RE2a the inner edge. RE1a was marked at the time when the field reaches the $-5\%B_d$ level, and RE2a is given by the end of the best fitting interval.

All of the time limits are detailed in Table 2 in UTC. With these, we defined the start and end times of each substructure by taking the midpoints of each error bar, setting the foot start at 9:48:49.8 ±0.9 s; the ramp start at 9:49:09.99 ±0.03 s; the ramp end at 9:49:10.11 ±0.03 s; and the overshoot end at 9:50:32 ±7 s. This times define the temporal widths shown on Table 3. In addition, we calculated the overshoot normalized amplitude as $(B_{max}-B_d)/B_d$, resulting in a 25 % increase over the downstream nominal value. To measure B_{max} we used the averaged magnetic field strength, sweeping from 10 s to 60 s time windows (1 to 6 upstream proton cyclotron period) until we measured a stable value. This way we avoided the effect of the high amplitude wave field (Mellott & Livesey, 1987; Tatrallyay et al., 1997).

4.1.3 Shock Speed and Spatial Length-scales

The shock velocity relative to the spacecraft and along the shock normal $\hat{N}$ (see section 4.1.1) was estimated from the method described in Gosling and Thomsen (1985), as indicated in section 3. To somehow account for the self-reforming nature of the Q⊥ supercritical shock, we computed a range of shock speeds considering different stages of foot formation. The full temporal width was used to calculate the speed for a 100% developed foot, and fractions of this width were used to compute the speed at lower formation stages. Then, the experimental foot widths were calculated in this velocity range and compared with the upper limit set by the analytical prediction of the model. For this crossing, we have an upper limit of 0.64 r_{ci} (where r_{ci} is the upstream local proton convected gyroradius given in Table 1).

Only foot width values below the theoretical limit were kept (as the specular reflection model is already an overestimation, Gosling & Thomsen, 1985). This meant only widths associated with a 99% to 100% formation stages remained, with shock velocities ranging from 15.4 km/s to 15.2 km/s. A low shock speed was expected, considering multi-spacecraft Earth studies by Meziane et al. (2014, 2015) that report a maximum of the velocity probability density function close to a few km/s in the absence of SW transients like dynamic pressure pulses. This was confirmed by the observation of steady space weather conditions in consecutive orbits, with no evidence of any short-term effect that could mean a significant increase in the dynamic pressure or EUV radiation (Modolo et al., 2006; Meziane et al., 2014, 2015; Hall et al., 2016; Gruesbeck et al., 2018). In addition, our calculated shock speeds are comparable with the $\sim$ 5 km/s estimation reported by Madanian et al. (2020) for a Martian shock. Though their shock is an order of magnitude slower than ours, both are still in a low speed regime.

Within the remaining shock speed values, we computed a range of widths for all three substructures. Considering the variations between the minimum and maximum values obtained, we calculated a final estimation for the foot, ramp and overshoot thicknesses summarized in Table 3. The relative sizes of each substructure can be seen in Figure 3, where we show the spatial magnetic field profile in different physically relevant length-scales.

We measured a completely developed foot smaller than the upstream local Larmor radius, which is compatible with the specularly reflected model of foot formation. Our results are similar to Earth studies by Mazelle and Lembège (2020) , who show that the foot width often falls under Woods (1971) turnaround distance of 0.68 r_{ci} for strictly perpendicular shocks with normal incidence SW. However, this is not a strict upper bound for all shock geometries, as Gosling and Thomsen (1985) analytical foot width prediction can yield values greater than 0.68 r_{ci} when there is departure from strictly perpendicular geometry.

The observed ramp width agrees with Earth studies by Mazelle et al. (2010), falling under their reported most probable values with ramp thicknesses below 5 c/ω_{pe}. It is also in agreement with Giagkiozis et al. (2017), who reported a (3.4±1.4) c/ω_{pe} ramp for a Venusian shock. Our work further supports that the shock ramp of Q⊥ supercritical shocks has a thickness of a few electron inertial lengths, and not of the order of the ion inertia length (Russell & Greenstadt, 1979; Scudder et al., 1986; Bale et al., 2005; Achilleos et al., 2006; Newbury & Russell, 1996).

As for the overshoot, results are compatible with Earth observations by Mellott and Livesey (1987), who reported overshoots with most probable thicknesses between 1 and 3 r_{ci}, as well as with previous studies on Mars by Tatrallyay et al. (1997), who considered a static Martian bow shock and reported overshoot widths between 0.5 to 2.5 r_{ci}. The similarities with Tatrallyay et al. (1997) results for a static shock layer could be related to the low speed of the Martian shock for the case reported here.

4.2 Jan 4, 2015 event

We analyzed a second case study on January 4, 2015, with a shock crossing at 3:18:26 UTC and $SZA = 69°$. The selected upstream and downstream intervals are 3:13:34.7 - 3:17:43.5 UTC and 3:25:50 - 3:27:40 UTC, respectively. These regions are shaded in Figure 4, where an alternative potential downstream interval is also shown further inside the magnetosheath, between 3:28:34.6 - 3:34:50.0 UTC. Between these two, we decided for the earliest interval, as the fields values already seem to plateau and the closeness to the shock jump is critical to guarantee the best downstream state description of the plasma transformed at the observed shock layer.

Table 1 summarizes the average upstream and downstream plasma and field parameters. To isolate the core proton distribution to compute the upstream ion temperature, we limited to the energy range between 250 - 2100 eV. In addition, we obtained a cone angle $\alpha_{cone} = 67°$, and an upstream Alfvén, sound, and fast magnetosonic speeds $V_A = 76$ km/s, $V_{cs} = 68$ km/s and $V_f = 105$ km/s. Alpha particles constitute 2% of the total ion number density. This translates into a $\sim$ 10% contribution to the total ion mass density, which lowers the Alfvén speed in about 4 km/s from the value obtained with the core protons only. The shock normal vector is $\hat{N} = (0.736, 0.362, -0.568)$, which has a 10° uncertainty and forms a shock normal angle $\theta_{B_uN} = (81 \pm 3)°$. This vector was used to compute the shock's Mach numbers that are $M_A = 4.7$, $M_{cs} = 5.3$ and $M_f = 3.4$, indicating a supercritical plasma regime.

The substructures delimitation in the time series is shown on Figure 5 and the time limits are detailed in Table 2. These times define a foot start at 3:17:52.2 ±0.1 s; a ramp start at 3:18:24.1 ±0.8 s; a ramp end at 3:18:27.88 ±0.09 s; and an overshoot end at 2:20:43 ±7 s. The temporal and spatial widths are shown on Table 3 and the relative sizes are shown in Figure 3. The spatial widths were obtained for a shock speed around 20 km/s and a theoretical foot width upper limit of 0.695 r_{ci} (Gosling & Thomsen, 1985). These results are similar to those obtained for the first event. In particular, we see an example of how the foot thickness is not limited by Woods (1971) 0.68 r_{ci} turnaround distance, since θ_{Bn} is not exactly 90° and $\theta_{Vn} \neq 0°$. The ramp is wider than that from the previous shock crossing but is still less than half the ion inertial length. Moreover, the estimated overshoot width supports our choice of the asymptotic downstream region closer to the shock jump, and the subsequent delimitation of the overshoot end error bar in the time series.

5 Final Remarks and Conclusions

In this work we report on the identification and first complete characterization of the Martian quasi-perpendicular supercritical substructures assuming a constant-velocity moving shock front, using MAVEN plasma and magnetic field data. We not only present new results in the characterization of the Martian shock structure, but we also provide a meticulous analysis methodology that stresses the importance on the correct processing of MAVEN data, and the clarity and consistency of the criteria used in the data selection and analysis. We pay special attention to the determination of the entry to the ion foot and the identification of the main and secondary overshoots, where the presence of the ULF waves (generated from the pick-up of exospheric ions) could mean an erroneous identification of these shock features. We also attempt to somehow account for the non-stationarity and reformation of the shock, even with the limitations of a single spacecraft mission, by computing a range of local shock speeds to obtain the substructures spatial widths from the timeseries.

We have found that, despite the particular nature of the Martian plasma environment, the structure of supercritical quasi-perpendicular shocks is in many ways comparable with that of the Terrestrial shock, which presents a substantially different solar wind – planet interaction. We observed a shock foot smaller than the upstream proton convected gyroradius, compatible with the model of specular reflection of foot formation (Gosling & Thomsen, 1985) and Earth observations by Mazelle and Lembège (2020). We found that the shock ramp is typically very narrow, of the order of a few electron inertial lengths, which agrees with studies on the Terrestrial (Mazelle et al., 2010) and Venusian shocks (Giagkiozis et al., 2017), and further supports that the ramp of supercritical quasi-perpendicular shocks is smaller than the ion inertial length (Russell & Greenstadt, 1979; Scudder et al., 1986; Bale et al., 2005; Achilleos et al., 2006; Newbury & Russell, 1996). Moreover, we observed an overshoot of a few proton convected gyroradii, as reported for the Earth bow shock by Mellott and Livesey (1987) and previous studies of the Martian shock under the assumption of a static boundary (Tatrallyay et al., 1997).

The similarities with the Earth show that the core solar wind protons dynamic seems to play the major role on the Martian shock structure despite the small size of the boundary. However, the narrower magnetosheath does mean these kinetic effects are less effective in the plasma thermalization. Downstream from the shock the plasma does not fully thermalize, even with the presence of other sources of free energy like the ULF waves, which provide a wave - particle interaction that one could think would contribute to the energy dissipation. However, they do not seem to be significantly efficient to modify the shock structure, though they do make it considerably more complex to separate one from the other.

This raises the question if the main differences in the Martian environment (small size, large curvature, mass-loading, pick-up of exospheric ions) have any influence on the supercritical substructures at all, or if there is some intrinsic nature for this type of shocks when it comes to their characteristic length-scales. However, to fully answer this question we must extend this analysis to other shock crossings and gain insight into the statistical variations. This is the scope of a future work.

Acknowledgments

All data used are publicly available on the NASA Planetary Data System (https://pds.nasa.gov), under Search Data, MAVEN Mission, Planetary Plasma Interactions Node. The authors would like to thank the LIA-MAGNETO, CNRS-CONICET collaboration. S.B. is a CONICET PhD fellow. The authors acknowledge financial support from the Agencia de Promoción Científica y Tecnológica (Argentina) through grants PICT 1707-2015 and 1103-2018.

References

Achilleos, N., Bertucci, C., Russell, C., Hospodarsky, G., Rymer, A., Arridge, C., ... others (2006). Orientation, location, and velocity of saturn's bow shock: Initial results from the cassini spacecraft. *Journal of Geophysical Research: Space Physics*, *111*(A3). doi: 10.1029/2005JA011297

Acuña, M., Connerney, J., Wasilewski, P. a., Lin, R., Anderson, K., Carlson, C., ... others (1998). Magnetic field and plasma observations at mars: Initial results of the mars global surveyor mission. *Science*, *279*(5357), 1676–1680. doi: 10.1126/science.279.5357.1676

Bale, S., Balikhin, M., Horbury, T., Krasnoselskikh, V., Kucharek, H., Möbius, E., ... others (2005). Quasi-perpendicular shock structure and processes. *Space science reviews*, *118*(1-4), 161–203. doi: 10.1007/s11214-005-3827-0

Bertucci, C., Hamilton, D., Kurth, W., Hospodarsky, G., Mitchell, D., Sergis, N., ... Dougherty, M. (2015). Titan's interaction with the supersonic solar wind. *Geophysical Research Letters*, *42*(2), 193–200. doi: 10.1002/2014GL062106

Burgess, D. (1995). Collisionless shocks. *Introduction to space physics*, 129–163.

Connerney, J., Espley, J., Lawton, P., Murphy, S., Odom, J., Oliversen, R., & Sheppard, D. (2015b). The maven magnetic field investigation. *Space Science Reviews*, *195*(1-4), 257–291. doi: 10.1007/s11214-015-0169-4

Connerney, J., Espley, J. R., DiBraccio, G. A., Gruesbeck, J., Oliversen, R., Mitchell, D., ... Jakosky, B. (2015a). First results of the maven magnetic field investigation. *Geophysical Research Letters*, *42*(21), 8819–8827. doi: 10.1002/2015GL065366

Delva, M., & Dubinin, E. (1998). Upstream ulf fluctuations near mars. *Journal of Geophysical Research: Space Physics*, *103*(A1), 317–326. doi: 10.1029/97JA02501

Dimmock, A. P., Russell, C. T., Sagdeev, R. Z., Krasnoselskikh, V., Walker, S. N., Carr, C., ... others (2019). Direct evidence of nonstationary collisionless shocks in space plasmas. *Science advances*, *5*(2), eaau9926. doi: 10.1126/sciadv.aau9926

Edmiston, J., & Kennel, C. (1984). A parametric survey of the first critical mach number for a fast mhd shock. *Journal of plasma physics*, *32*(3), 429–441. doi: 10.1017/S002237780000218X

Fränz, M., Dubinin, E., Roussos, E., Woch, J., Winningham, J., Frahm, R., ... Lundin, R. (2007). Plasma moments in the environment of mars. In *The mars plasma environment* (pp. 165–207). Springer. doi: 10.1007/978-0-387-70943-7_7

Giagkiozis, S., Walker, S. N., Pope, S. A., & Collinson, G. (2017). Validation of single spacecraft methods for collisionless shock velocity estimation. *Journal of Geophysical Research: Space Physics*, *122*(8), 8632–8641. doi: 10.1002/2017JA024502

Gosling, J., & Thomsen, M. (1985). Specularly reflected ions, shock foot thicknesses, and shock velocity determinations in space. *Journal of Geophysical Research: Space Physics*, *90*(A10), 9893–9896. doi: 10.1029/JA090iA10p09893

Gruesbeck, J. R., Espley, J. R., Connerney, J. E., DiBraccio, G. A., Soobiah, Y. I., Brain, D., ... Mitchell, D. L. (2018). The three-dimensional bow shock of mars as observed by maven. *Journal of Geophysical Research: Space Physics*, *123*(6), 4542–4555. doi: 10.1029/2018JA025366

Hada, T., Oonishi, M., Lembège, B., & Savoini, P. (2003). Shock front nonstationarity of supercritical perpendicular shocks. *Journal of Geophysical Research: Space Physics*, *108*(A6). doi: 10.1029/2002JA009339

Halekas, J., Ruhunusiri, S., Harada, Y., Collinson, G., Mitchell, D., Mazelle, C., ... others (2017). Structure, dynamics, and seasonal variability of the mars-solar wind interaction: Maven solar wind ion analyzer in-flight performance and science results. *Journal of Geophysical Research: Space Physics*, *122*(1), 547–578. doi: 10.1002/2016JA023167

Halekas, J., Taylor, E., Dalton, G., Johnson, G., Curtis, D., McFadden, J., ... Jakosky, B. (2015). The solar wind ion analyzer for maven. *Space Science Reviews*, *195*(1-4), 125–151. doi: 10.1007/s11214-013-0029-z

Hall, B. E. S., Lester, M., Sánchez-Cano, B., Nichols, J. D., Andrews, D. J., Edberg, N. J., ... others (2016). Annual variations in the martian bow shock location as observed by the mars express mission. *Journal of Geophysical Research:*

Space Physics, *121*(11), 11–474. doi: 10.1002/2016JA023316

Horbury, T., Cargill, P., Lucek, E., Eastwood, J., Balogh, A., Dunlop, M., … Georgescu, E. (2002). Four spacecraft measurements of the quasiperpendicular terrestrial bow shock: Orientation and motion. *Journal of Geophysical Research: Space Physics*, *107*(A8), SSH–10. doi: 10.1029/2001JA000273

Jakosky, B. M., Lin, R., Grebowsky, J., Luhmann, J., Mitchell, D., Beutelschies, G., … others (2015). The mars atmosphere and volatile evolution (maven) mission. *Space Science Reviews*, *195*(1-4), 3–48. doi: 10.1007/s11214-015-0139-x

Kantrowitz, A., Petschek, H., & Kunkel, W. (1966). Plasma physics in theory and application. *McGraw-Hill Book Company, New York*, *147*.

Lembège, B., Savoini, P., Hellinger, P., & Trávníček, P. M. (2009). Nonstationarity of a two-dimensional perpendicular shock: Competing mechanisms. *Journal of Geophysical Research: Space Physics*, *114*(A3). doi: 10.1029/2008JA013618

Leroy, M. (1983). Structure of perpendicular shocks in collisionless plasma. *The Physics of fluids*, *26*(9), 2742–2753. doi: 10.1063/1.864468

Leroy, M., Goodrich, C., Winske, D., Wu, C., & Papadopoulos, K. (1981). Simulation of a perpendicular bow shock. *Geophysical Research Letters*, *8*(12), 1269–1272. doi: 10.1029/GL008i012p01269

Leroy, M., Winske, D., Goodrich, C., Wu, C. S., & Papadopoulos, K. (1982). The structure of perpendicular bow shocks. *Journal of Geophysical Research: Space Physics*, *87*(A7), 5081–5094. doi: 10.1029/JA087iA07p05081

Livesey, W., Kennel, C., & Russell, C. (1982). Isee-1 and-2 observations of magnetic field strength overshoots in quasi-perpendicular bow shocks. *Geophysical Research Letters*, *9*(9), 1037–1040. doi: 10.1029/GL009i009p01037

Livesey, W., Russell, C., & Kennel, C. (1984). A comparison of specularly reflected gyrating ion orbits with observed shock foot thicknesses. *Journal of Geophysical Research: Space Physics*, *89*(A8), 6824–6828. doi: 10.1029/JA089iA08p06824

Madanian, H., Schwartz, S. J., Halekas, J. S., & Wilson III, L. B. (2020). Nonstationary quasiperpendicular shock and ion reflection at mars. *Geophysical Research Letters*, *47*(11), e2020GL088309. doi: 10.1029/2020GL088309

Marshall, W. (1955). The structure of magneto-hydrodynamic shock waves. *Proceedings of the Royal Society of London. Series A. Mathematical and Physical Sciences*, *233*(1194), 367–376. doi: 10.1098/rspa.1955.0272

Mazelle, C., & Lembège, B. (2020). Evidence of the nonstationarity of the terrestrial bow shock from multi-spacecraft observations: Methodology, results and quantitative comparison with pic simulations. *Annales Geophysicae Discussions*, 1–45.

Mazelle, C., Lembège, B., Morgenthaler, A., Meziane, K., Horbury, T., Génot, V., … Dandouras, I. (2010). Self-reformation of the quasi-perpendicular shock: Cluster observations. In *Aip conference proceedings* (Vol. 1216, pp. 471–474). doi: 10.1063/1.3395905

Mazelle, C., Meziane, K., Mitchell, D., Garnier, P., Espley, J., Hamza, A., … Jakosky, B. (2018). Evidence for neutrals-foreshock electrons impact at mars. *Geophysical Research Letters*, *45*(9), 3768–3774. doi: 69910.1002/2018GL077298

Mazelle, C., Winterhalter, D., Sauer, K., Trotignon, J., Acuña, M., Baumgärtel, K., … others (2004). Bow shock and upstream phenomena at mars. *Space Science Reviews*, *111*(1-2), 115–181. doi: 10.1023/B:SPAC.0000032717.98679.d0

Mellott, M., & Livesey, W. (1987). Shock overshoots revisited. *Journal of Geophysical Research: Space Physics*, *92*(A12), 13661–13665. doi: 10.1029/JA092iA12p13661

Meziane, K., Alrefay, T., & Hamza, A. (2014). On the shape and motion of the earth's bow shock. *Planetary and Space Science*, *93*, 1–9. doi: 10.1016/j.pss.2014.01.006

Meziane, K., Hamza, A., Maksimovic, M., & Alrefay, T. (2015). The earth's bow shock velocity distribution function. *Journal of Geophysical Research: Space Physics*, *120*(2), 1229–1237. doi: 10.1002/2014JA020772
Meziane, K., Mazelle, C., Romanelli, N., Mitchell, D., Espley, J., Connerney, J., ... Jakosky, B. (2017). Martian electron foreshock from maven observations. *Journal of Geophysical Research: Space Physics*, *122*(2), 1531–1541. doi: 10.1002/2016JA023282
Meziane, K., Mazelle, C. X., Mitchell, D., Hamza, A., Penou, E., & Jakosky, B. (2019). A fast fermi acceleration at mars bow shock. *Journal of Geophysical Research: Space Physics*, *124*(7), 5528–5538. doi: 10.1029/2019JA026614
Mitchell, D., Mazelle, C., Sauvaud, J.-A., Thocaven, J.-J., Rouzaud, J., Fedorov, A., ... others (2016). The maven solar wind electron analyzer. *Space Science Reviews*, *200*(1-4), 495–528. doi: 10.1007/s11214-015-0232-1
Modolo, R., Chanteur, G., Dubinin, E., & Matthews, A. (2006). Simulated solar wind plasma interaction with the martian exosphere: influence of the solar euv flux on the bow shock and the magnetic pile-up boundary.
Moses, S., Coroniti, F., Kennel, C., Scarf, F., Greenstadt, E., Kurth, W., & Lepping, R. (1985). High time resolution plasma wave and magnetic field observations of the jovian bow shock. *Geophysical research letters*, *12*(4), 183–186. doi: 10.1029/GL012i004p00183
Moses, S., Coroniti, F., & Scarf, F. (1988). Expectations for the microphysics of the mars-solar wind interaction. *Geophysical Research Letters*, *15*(5), 429–432. doi: 10.1029/GL015i005p00429
Newbury, J., & Russell, C. (1996). Observations of a very thin collisionless shock. *Geophysical research letters*, *23*(7), 781–784. doi: 10.1029/96GL00700
Paschmann, G., Sckopke, N., Bame, S., & Gosling, J. (1982). Observations of gyrating ions in the foot of the nearly perpendicular bow shock. *Geophysical Research Letters*, *9*(8), 881–884. doi: 10.1029/GL009i008p00881
Russell, C., & Greenstadt, E. (1979). Initial isee magnetometer results: Shock observation. *Space Science Reviews*, *23*(1), 3–37. doi: 10.1007/BF00174109
Russell, C., Luhmann, J., & Phillips, J. (1985). The location of the subsolar bow shock of venus: Implications for the obstacle shape. *Geophysical research letters*, *12*(10), 627–630. doi: 10.1029/GL012i010p00627
Russell, C., Luhmann, J., Schwingenschuh, K., Riedler, W., & Yeroshenko, Y. (1990). Upstream waves at mars: Phobos observations. *Geophysical Research Letters*, *17*(6), 897–900. doi: 10.1029/GL017i006p00897
Sagdeev, R., Shapiro, V., Shevchenko, V., Zacharov, A., Kiraly, P., Szego, K., ... Grard, R. (1990). Wave activity in the neighborhood of the bowshock of mars. *Geophysical research letters*, *17*(6), 893–896. doi: 10.1029/GL017i006p00893
Schwartz, S. J. (1998). Shock and discontinuity normals, mach numbers, and related parameters. *ISSI Scientific Reports Series*, *1*, 249–270.
Schwingenschuh, K., Riedler, W., Lichtenegger, H., Yeroshenko, Y., Sauer, K., Luhmann, J., ... Russell, C. (1990). Martian bow shock: Phobos observations. *Geophysical research letters*, *17*(6), 889–892. doi: 10.1029/GL017i006p00889
Sckopke, N., Paschmann, G., Bame, S., Gosling, J., & Russell, C. (1983). Evolution of ion distributions across the nearly perpendicular bow shock: Specularly and non-specularly reflected-gyrating ions. *Journal of Geophysical Research: Space Physics*, *88*(A8), 6121–6136. doi: 10.1029/JA088iA08p06121
Scudder, J., Mangeney, A., Lacombe, C., Harvey, C., Aggson, T., Anderson, R., ... Russell, C. (1986). The resolved layer of a collisionless, high β, supercritical, quasi-perpendicular shock wave: 1. rankine-hugoniot geometry, currents, and stationarity. *Journal of Geophysical Research: Space Physics*, *91*(A10), 11019–11052. doi: 10.1029/JA091iA10p11019
Smith, E. J., Davis, L., Coleman, P. J., & Jones, D. E. (1965). Magnetic field measurements near mars. *Science*, *149*(3689), 1241–1242. doi: 10.1126/science.149

.3689.1241

Sonnerup, B. U., & Scheible, M. (1998). Minimum and maximum variance analysis. *Analysis methods for multi-spacecraft data*, 185–220.

Sulaiman, A., Masters, A., Dougherty, M., Burgess, D., Fujimoto, M., & Hospodarsky, G. (2015). Quasiperpendicular high mach number shocks. *Physical review letters*, *115*(12), 125001. doi: 10.1103/PhysRevLett.115.125001

Tatrallyay, M., Gévai, G., Apathy, I., Schwingenschuh, K., Zhang, T.-L., Kotova, G., … Rosenbauer, H. (1997). Magnetic field overshoots in the martian bow shock. *Journal of Geophysical Research: Space Physics*, *102*(A2), 2157–2163. doi: 10.1029/96JA00073

Treumann, R. (2009). Fundamentals of collisionless shocks for astrophysical application, 1. non-relativistic shocks. *The Astronomy and Astrophysics Review*, *17*(4), 409–535. doi: 10.1007/s00159-009-0024-2

Vignes, D., Mazelle, C., Reme, H., Acuña, M., Connerney, J., Lin, R., … Ness, N. (2000). The solar wind interaction with mars: Locations and shapes of the bow shock and the magnetic pile-up boundary from the observations of the mag/er experiment onboard mars global surveyor. *Geophysical Research Letters*, *27*(1), 49–52. doi: 10.1029/1999GL010703

Woods, L. (1969). On the structure of collisionless magneto—plasma shock waves at super—critical alfvén—mach numbers. *Journal of Plasma Physics*, *3*(3), 435–447. doi: 10.1017/S0022377800004517

Woods, L. (1971). On double-structured, perpendicular, magneto-plasma shock waves. *Plasma Physics*, *13*(4), 289. doi: 10.1088/0032-1028/13/4/302

Yang, Z., Lu, Q., Gao, X., Huang, C., Yang, H., Liu, Y., … Han, D. (2013). Magnetic ramp scale at supercritical perpendicular collisionless shocks: Full particle electromagnetic simulations. *Physics of Plasmas*, *20*(9), 092116. doi: 10.1063/1.4821825

Yang, Z., Lu, Q., Lembège, B., & Wang, S. (2009). Shock front nonstationarity and ion acceleration in supercritical perpendicular shocks. *Journal of Geophysical Research: Space Physics*, *114*(A3). doi: 10.1029/2008JA013785

Zakharov, A. (1992). The plasma environment of mars: Phobos mission results. *GMS*, *66*, 327–344. doi: 10.1029/GM066p0327

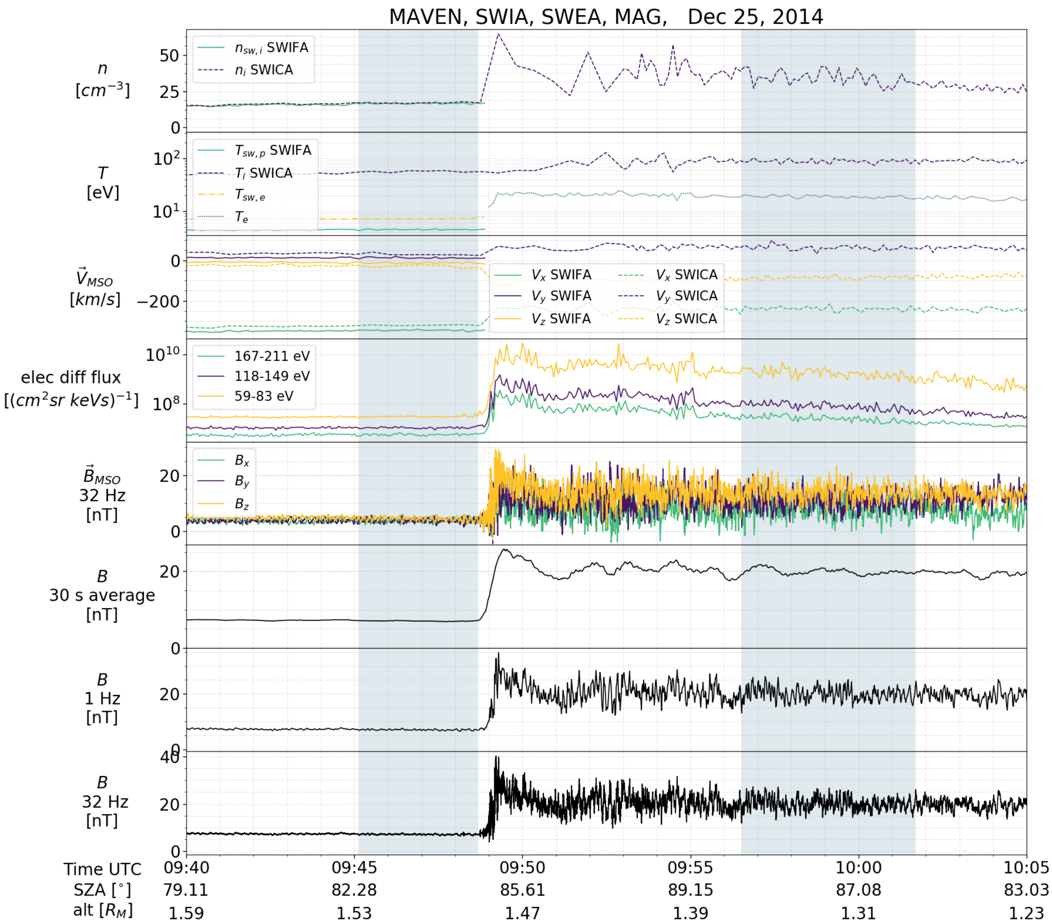

Figure 1. The Martian shock as seen by MAVEN MAG, SWIA and SWEA on December 25, 2014. Shaded intervals correspond to the upstream and downstream regions.

Table 1. Plasma and field parameters calculated in the selected upstream and downstream intervals of each shock crossing. Vector quantities are given in MSO coordinates. ω_{ci} is the proton cyclotron frequency, τ_{ci} the proton cyclotron period, c/ω_{pe} and c/ω_{pi} are the electron and ion inertial lengths, and $r_{ci} = |V_i|/\omega_{ci}$ is the local proton convected gyroradius.

	Dec 25, 2014		Jan 4, 2015	
	Upstream 9:45:07 - 9:48:41 UTC	Downstream 9:56:31 - 10:01:42 UTC	Upstream 3:13:34.7 - 3:17:43.5 UTC	Downstream 3:25:50.0 - 3:27:40.0 UTC
$\mathbf{B}_{X_{MSO}}$ $[nT]$	3.9 ± 0.7	8 ± 3	-1.8 ± 0.5	-2 ± 1
$\mathbf{B}_{Y_{MSO}}$ $[nT]$	3.8 ± 0.7	11 ± 3	5.0 ± 0.4	-16.3 ± 0.9
$\mathbf{B}_{Z_{MSO}}$ $[nT]$	4.4 ± 0.7	14 ± 3	-0.6 ± 0.7	6 ± 1
$\|\mathbf{B}\|$ $[nT]$	7.1 ± 0.2	20 ± 3	5.5 ± 0.2	18 ± 1
$\mathbf{V}_{i,X_{MSO}}$ $[km/s]$	-345 ± 2	-242 ± 10	-501 ± 5	-295 ± 13
$\mathbf{V}_{i,Y_{MSO}}$ $[km/s]$	12 ± 3	63 ± 11	35 ± 8	121 ± 11
$\mathbf{V}_{i,Z_{MSO}}$ $[km/s]$	-12 ± 3	-85 ± 7	6 ± 6	-141 ± 14
$\|\mathbf{V}_i\|$ $[km/s]$	346 ± 2	264 ± 10	503 ± 5	349 ± 16
T_i $[eV]$	4.4 ± 0.1	89 ± 7	17.5 ± 0.9	169 ± 18
T_e $[eV]$	7	19	13.5 ± 0.4	43 ± 3
n_i $[cm^{-3}]$	16.6 ± 0.5	34 ± 5	2.2 ± 0.1	4.1 ± 0.4
n_e $[cm^{-3}]$	15.3 ± 0.3	33 ± 5	2.06 ± 0.06	7 ± 1
β_p	0.60	3	0.53	0.9
β_e	0.97	0.65	0.40	0.23
ω_{ci} $[rad/s]$	0.68 ± 0.02	1.9 ± 0.2	0.52 ± 0.02	1.69 ± 0.09
τ_{ci} $[s]$	9.3 ± 0.3	3.3 ± 0.4	12.0 ± 0.5	3.7 ± 0.2
r_{ci} $[km]$	511 ± 16	138 ± 18	962 ± 38	207 ± 15
c/ω_{pe} $[km]$	1.30 ± 0.02	0.91 ± 0.06	3.6 ± 0.1	2.6 ± 0.1
c/ω_{pi} $[km]$	55.9 ± 0.8	39 ± 3	153 ± 5	112 ± 5

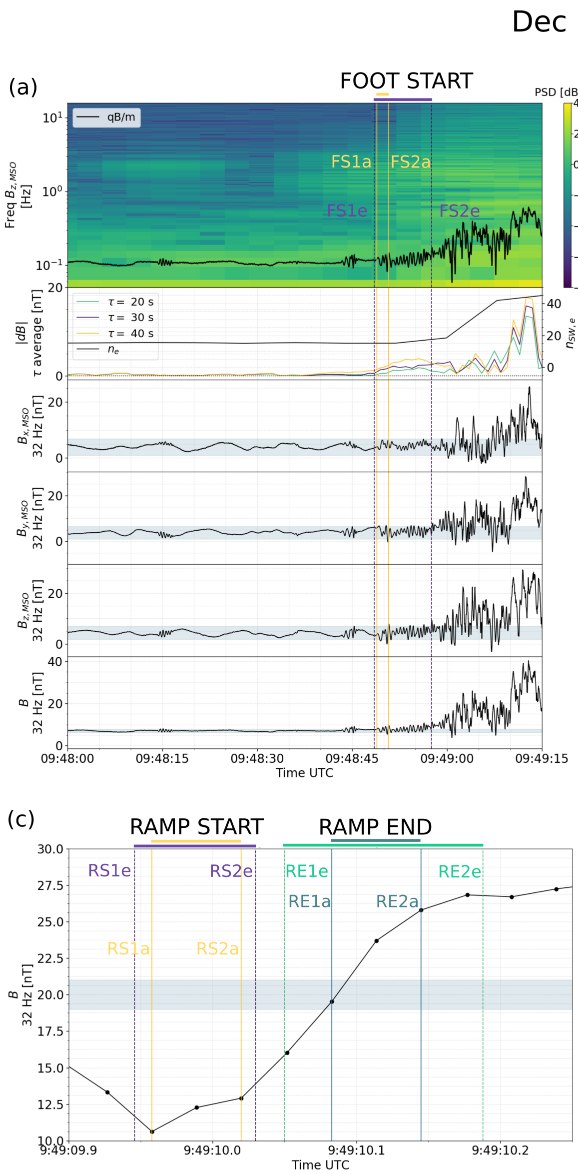

Figure 2. Substructures delimitation for the December 25, 2014 event. **(a)** Foot start. FS1e and FS2e are the foot start outer and inner edges selected by eye. FS1a and FS2a are the outer and inner edges selected with the automated algorithm. The shaded areas mark a $\pm 4\sigma$ variation from the mean upstream field values. **(b)** Overshoot end. OE1e and OE2e are the overshoot end outer and inner edges selected by eye. OE1a and OE2a are the outer and inner edges selected with the automated algorithm. The shaded areas mark a $\pm 5\% B_d$ margin, where B_d is the downstream averaged field. **(c)** Ramp start and ramp end. RS1e and RS2e are the ramp start outer and inner edges selected by eye, and RE1e and RE2e are the ramp end outer and inner edges selected by eye. RS1a and RS2a are the ramp start outer and inner edges selected by the automated algorithm, and RE1a and RE2a are the ramp end outer and inner edges selected by the automated algorithms.

Table 2. Time limits, in UTC, for the visually- and automated-delimited start and end error bars of each substructure.

	Dec 25, 2014				Jan 4, 2015			
	visual		automated		visual		automated	
	outer edge	inner edge	outer edge	inner edge	outer edge	inner edge	outer edge	inner edge
foot start	9:48:48.5	9:48:57.5	9:48:48.9	9:49:50.8	3:17:51.1	3:17:56.5	3:17:52.1	3:17:52.3
ramp start/foot end	9:49:09.946	9:49:10.02978	9:49:09.958	9:49:10.020	3:18:23.3	3:18:25.6	3:18:23.312	3:18:24.969
ramp end/overshoot start	9:49:10.050	9:49:10.188	9:49:10.083	9:49:10.145	3:18:26.83	3:18:30.015	3:18:27.781	3:18:27.969
overshoot end	9:50:16.1	9:50:31.0	9:50:24.5	9:50:38.5	3:20:08.9	3:20:50.3	3:20:36.5	3:20:50.3

Table 3. Temporal and spatial widths of each substructure.

width	Dec 25, 2014			Jan 4, 2015		
	foot	ramp	overshoot	foot	ramp	overshoot
temporal	20 ± 1 s	0.13 ± 0.06 s	81 ± 7 s	31.9 ± 0.9 s	3.7 ± 0.9 s	136 ± 7 s
km	308 ± 16	2 ± 1	1244 ± 113	636 ± 22	74 ± 19	2695 ± 152
physical scales	$(0.60 \pm 0.04)\ r_{ci}$	$(1.5 \pm 0.7)\ c/\omega_{pe}$	$(2.4 \pm 0.2)\ r_{ci}$	$(0.66 \pm 0.03)\ r_{ci}$	$(21 \pm 5)\ c/\omega_{pe}$	$(2.8 \pm 0.2)\ r_{ci}$

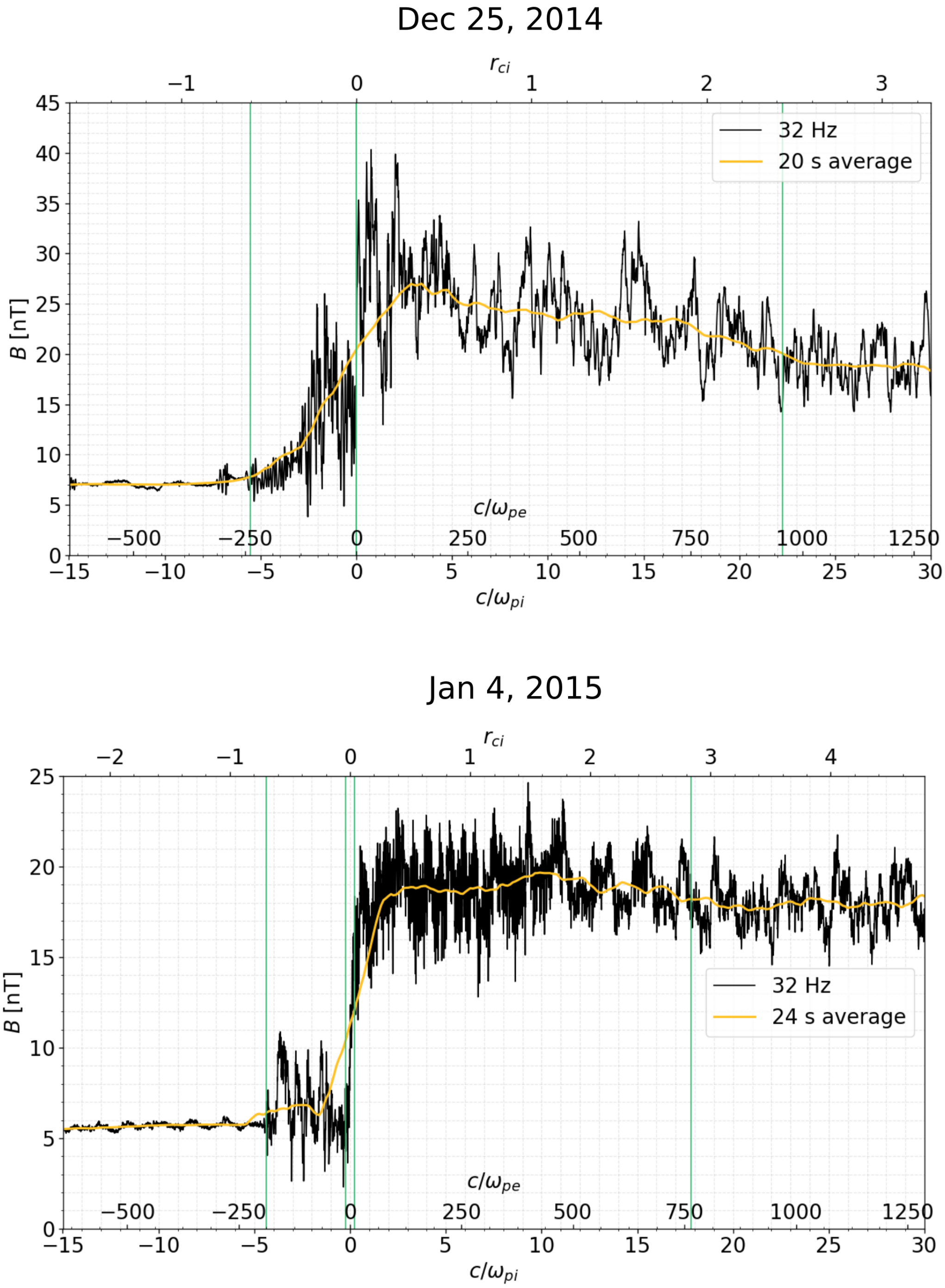

Figure 3. Spatial magnetic field profiles along the shock normal, in units of the upstream proton inertial length c/ω_{pi}, the upstream electron inertial length c/ω_{pe}, and the upstream proton convected gyroradius r_{ci}. Vertical lines delimit the foot, ramp and overshoot.

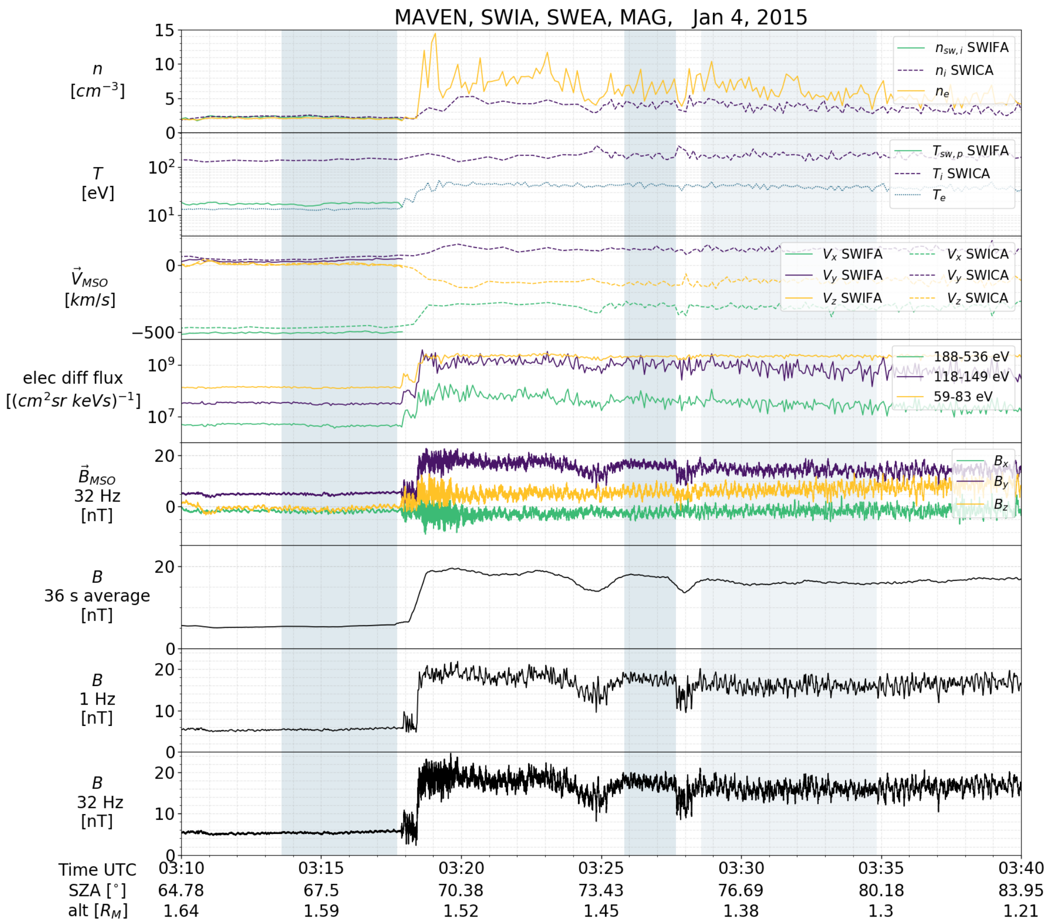

Figure 4. The Martian shock as seen by MAVEN MAG, SWIA and SWEA on January 4, 2015. Shaded intervals correspond to the upstream and downstream regions, where two potential downstream intervals are showcased.

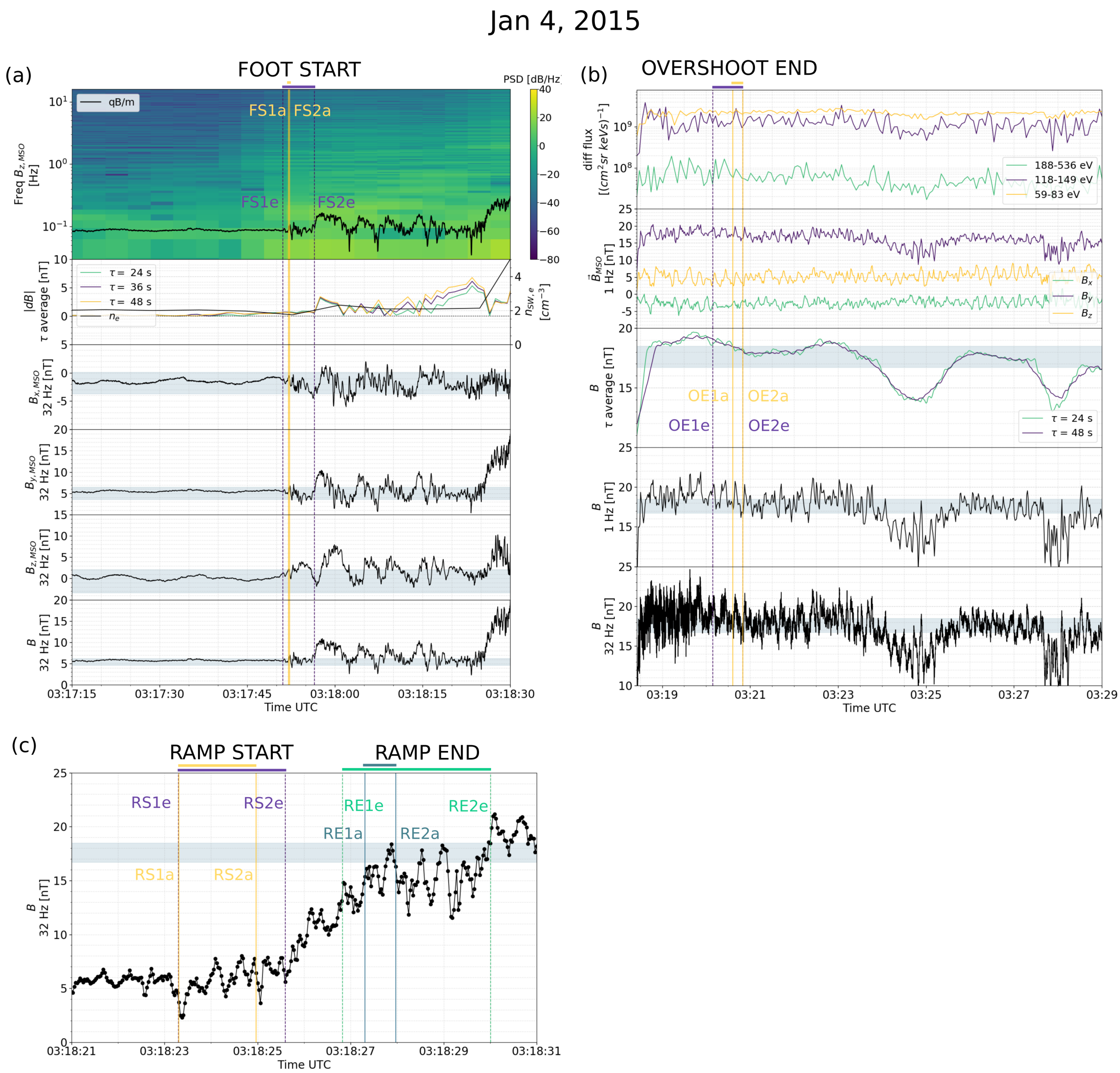

Figure 5. Substructures delimitation for the January 4, 2015 event. **(a)** Foot start. FS1e and FS2e are the foot start outer and inner edges, respectively, selected by eye. FS1a and FS2a are the outer and inner edges selected with the automated algorithm. The shaded areas mark a $\pm 4\sigma$ variation from the mean upstream field values. **(b)** Overshoot end. OE1e and OE2e are the overshoot end outer and inner edges selected by eye. OE1a and OE2a are the outer and inner edges selected with the automated algorithm. The shaded areas mark a $\pm 5\% B_d$ margin, where B_d is the downstream averaged field. **(c)** Ramp start and ramp end. RS1e and RS2e are the ramp start outer and inner edges selected by eye, and RE1e and RE2e are the ramp end outer and inner edges selected by eye. RS1a and RS2a are the ramp start outer and inner edges selected by the automated algorithm, and RE1a and RE2a are the ramp end outer and inner edges selected by the automated algorithms.